14th International Symposium on Turbulence and Shear Flow Phenomena (TSFP14)
Heidelberg, Germany, July 28–31, 2026

SPATIO-TEMPORAL FEATURES OF HEAT- AND MOMENTUM-TRANSFER IN IMPINGING JETS USING LSE-HPOD

M. Raiola,
Aerospace Engineering Department, Universidad Carlos III de Madrid, Av. Universidad 30, Leganés 28912, Spain
Institute of Fluid Mechanics, Karlsruhe Institute of Technology, Kaiserstraße 10, Karlsruhe D-76131, Germany
mraiola@ing.uc3m.es

F. Secchi, D. Gatti, J. Kriegseis and B. Frohnapfel
Institute of Fluid Mechanics, Karlsruhe Institute of Technology, Kaiserstraße 10, Karlsruhe D-76131, Germany

ABSTRACT

This work aims at identifying a relation between instantaneous heat and momentum transfer for spatiotemporally coherent features produced in the boundary layer of an impinging jet. This relation is identified from Direct Numerical Simulations data of an impinging jet with Pr=1, Re=5300 and wall-to-plate distance of 2. Matching heat- and momentum-transfer features acting as travelling waves in the radial direction have been extracted through space-only Hilbert proper orthogonal decomposition and linear stochastic estimation. The existence of matching waves suggests that a similarity holds between the two transfer phenomena in a time-varying scenario even in this complex flow configuration. Interestingly, a phase delay between the two wall fluxes is identified.

1 Introduction

Impinging jets are widely used in cooling applications due to their capability of determining localized and high heat transfer rates. They have been extensively exploited for cooling of electronics components, turbine blades, and in several other industrial applications. Their importance for cooling applications led the scientific community to correlate the average impinging-jet wall heat transfer to the main flow parameters, e.g. Reynolds number, the nozzle-to-plate distance, and conditions (Jambunathan *et al.*, 1992). The physical interplay between the instantaneous flow and the heat transfer, however, has not been equally explored and requires more detailed insights. One step in this direction is provided by Rönnberg & Duwig (2021), identifying the relation between flow structures convected in the radial direction and wall heat transfer using extended proper orthogonal decomposition (EPOD, Borée, 2003). For wall-bounded flows, the interplay between flow and heat transfer is typically regulated through the Reynolds analogy, which states that momentum and heat exchange occur similarly in a fluid flow with Prandtl number Pr=1. However impinging jets break the Reynolds analogy (Woodworth *et al.*, 2023), specifically within their stagnation region, even if downstream of it a return towards similar heat and momentum transfer might be expected (Wilke & Sesterhenn, 2017). In this work we analyze the relation between heat and momentum transfer in terms of traveling features for an impinging jet with Pr=1.

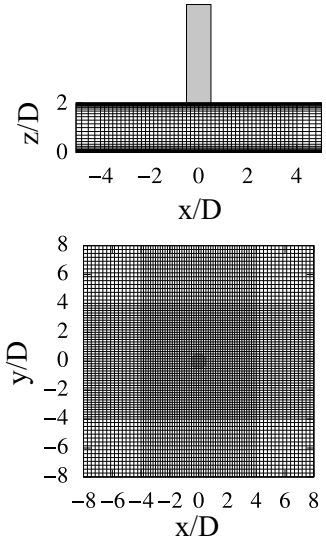


Figure 1. Computational domain: lateral view (top); top view (bottom). Only half of the mesh elements are included in this sketch.

2 Computational setup

We consider a turbulent jet issued from a fully-developed pipe flow with diameter D and bulk velocity U_b. The jet impinges on a plate located at distance 2D from the nozzle exit. The flow is confined by a second plate parallel to the impingement one, placed at the location of the nozzle exit, which prevents outer air entrainment.

For this flow, incompressible Navier-Stokes equations are considered with a $\mathrm{Re} = U_b D/\nu = 5300$, while a transport equation is included for the passive scalar field $\theta = (T - T_j)/(T_w - T_j)$, where T indicates the fluid temperature, T_j the exit jet temperature and T_w the prescribed wall temperature. The equations are integrated using the flow-solver Nek5000. The mesh used to discretize the computational domain (Fig. 1) contains 1168128 elements on which the solution is approximated using Lagrange polynomials of degree 7. A uniform in-plane elements distribution in the square [-4D, 4D] × [-4D, 4D] is used. No-slip boundary conditions for the velocity field are prescribed on the impingement and confinement

plates, whereas at the inflow section of the computational domain (i.e. at the nozzle exit section) a turbulent velocity field is interpolated at each time-step from a cross-section of a fully-developed turbulent pipe flow simulation. Dirichlet boundary conditions for the temperature are prescribed on the impingement and confinement plates and on the inflow section of the domain. The confinement plate is assumed to be in thermal equilibrium with the issued jet. On the lateral open boundaries of the computational domain, the energy-stable boundary conditions proposed by Dong (2015) and Liu *et al.* (2020) are applied, respectively, for velocity and temperature fields.

3 Data-reduction techniques

In this work, the instantaneous Nusselt number Nu, wall shear stress τ_w and wall pressure p distributions over the impingement plate are analyzed in order to identify spatio-temporal coherent features in the heat and momentum transfer. Given the central symmetry of the problem, these field quantities are expressed in a polar reference frame, with r and φ being the radial and azimuthal coordinates. Modal analysis is performed on the Nu maps by means of the Hilbert POD (HPOD, Raiola & Kriegseis, 2026), a complex-valued extension of the space-only POD. The analytic signal $\widetilde{\mathrm{Nu}}$ of the Nu maps is computed through the Hilbert transform in the radial direction, extending the dataset to complex values, before applying space-only POD, resulting in

$$\widetilde{\mathrm{Nu}}(r,\varphi,t) = \sum_i \psi_{q_i}(t)\sigma_i\phi_{q_i}(r,\varphi) \tag{1}$$

where σ_i, ψ_{q_i} and ϕ_{q_i} are, respectively, the real-valued singular value and complex-valued temporal pattern and spatial pattern associated to the i-th mode. HPOD modes are ranked in terms of σ_i, which is representative of the contribution of each mode to the variance in the dataset. The spatial pattern ϕ_i inherits the analytic-signal properties of the dataset, resulting in its real and imaginary parts being shifted by $\pi/2$ in the radial direction, i.e. it can be approximated as a complex exponential $A(r)\exp(jk_r r + jk_\varphi\varphi)$, with k_r and k_φ being the local radial and azimuthal wavenumbers, respectively. Note that the behaviour of the modes in the azimuthal direction can be reduced to a simple Fourier expansion due to the central symmetry, i.e. the azimuthal wavenumber does not depend on the spatial position. This allows to capture the travelling-wave features in the radial direction when the temporal pattern ψ_i assumes a form of the type $B(t)\exp(-j\omega t)$. It is worth remarking that HPOD allows to capture instantaneous/local modulation effects in the wave patterns, thus being akin to a time/space-frequency analysis.

The Nu decomposition is extended to τ_w and p on the impingement plate by means of Linear Stochastic Estimation (LSE), in a fashion similar to EPOD. The spatial patterns of τ_w and p linearly correlated in time to the spatial patterns ϕ_q of Nu are retrieved by projection of the τ_w and p datasets on the basis spanned by the HPOD temporal patterns ψ_q. This results in the decomposition

$$\begin{aligned} \tau_w(r,\varphi,t) &= \sum_i \psi_{q_i}(t)\sigma_{\tau_i}\phi_{\tau_i}(r,\varphi) \\ p(r,\varphi,t) &= \sum_i \psi_{q_i}(t)\sigma_{p_i}\phi_{p_i}(r,\varphi) \end{aligned} \tag{2}$$

where σ_{τ_i} and ϕ_{τ_i} are the pseudo singular values and spatial patterns of the quantity τ_w correlated to the i-th HPOD mode of Nu, while σ_{p_i} and ϕ_{p_i} are the ones associated to p.

4 Preliminary results

The results of the LSE-HPOD decomposition are presented in Fig. 2 to Fig. 5 for the 1st to 4th HPOD modes. The 1st column of each figure represents the HPOD spatial pattern ϕ_q of Nu, expressed in terms of its real, imaginary and absolute value parts (from top to bottom). These patterns correspond to approximately 16.8%, 14.2%, 14.1%, and 13.5% of the Nu dataset standard deviation (std), respectively. The spatial patterns show a wave pattern in the radial direction, with real and imaginary parts shifted by $\pi/2$ due to the analytic-signal properties. The most intense activity is produced approximately in $r/D \in [1,2]$, as shown by the absolute value map. The 2nd and 3rd columns presents the spatial patterns ϕ_τ and ϕ_p of τ_w and p, respectively. These patterns correspond respectively to the 11.4%, 5.9%, 9.6%, and 13.6% of the std of τ_w and to the 11.4%, 5.9%, 9.3%, and 14.6% of the std of p. These patterns show great resemblance to the one of Nu, mimicking similar behavior — even if smoother — in the azimuthal direction. Finally, the 4th row shows the time-frequency spectrogram of the HPOD temporal patterns. The green line represents the instantaneous maximum of the spectrogram. The spectrogram confirms that, despite the intermittency in time, the instantaneous frequency content is band-limited around a fixed Strouhal number (St ≈ 0.70 for i=1, St ≈ 0.75 for i=2, St ≈ 0.62 for i=3 and St ≈ 0.49 for i=4). This reinforces the idea that the retrieved features act as travelling waves in the radial direction.

The main differences between the patterns of Nu and the ones of τ_w and p is related to a shift of the waves in the radial direction. To visualize more clearly this behavior, a Fourier decomposition in the azimuthal direction is applied to both Nu, τ_w and p spatial patterns. The first 4 azimuthal wavenumbers k_φ of this decomposition are reported in Fig. 6 for mode numbers $i \in [1,4]$, isolating the radial wavepattern from the azimuthal Fourier expansion. In order to correctly represent the relevance of these patterns in the data, they have been rescaled with respect to their relative importance in terms of std in their respective dataset. For all the modes each azimuthal wavenumber corresponds to a modulated radial wave. Waves of different quantities seem to match in terms of shape and wavelengths (corresponding to 0.5D in most cases), mainly differing by a phase shift between them. The spatial modulation of the waves can be extracted from the envelope of their complex-valued representation, i.e. its absolute value, reported in Fig. 7. This envelope can be considered as the region of space where the activity of the wave pattern is most prominent. The envelopes of waves of different quantities match in most of the cases, indicating that they go through similar spatial modulation. This suggests that the phase shift observed in the "carrier" - i.e. the high-frequency part of the wave subjected to the modulation - is not intrinsically a spatial phenomenon but rather a spatiotemporal shift. Due to the nature of the LSE analysis technique, the temporal evolution of the modes of different quantities is fixed to follow the same exact temporal function, which does not allow any temporal shift between different quantities. Different timings of the effect of flow structures passing over the plate must be therefore captured through spatial shift of the spatiotemporally coherent waves. In general, the waves extracted seem to be mostly active for $r/D \in [1,2]$, especially for the leading modes and the lowest azimuthal wavenumbers. This is compatible with these

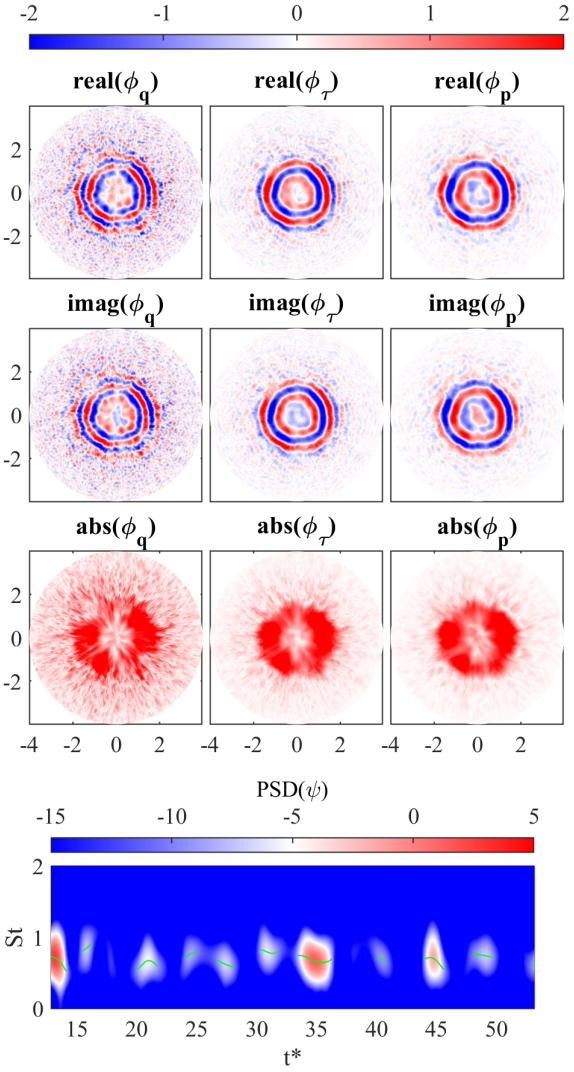


Figure 2. 1st LSE-HPOD mode. Spatial patterns of Nu (1st column), τ_w (2nd column) and p (3rd column), represented as real (1st row), imaginary (2nd row) and absolute value (3rd row) parts. Spectrogram of the temporal pattern (4th row).

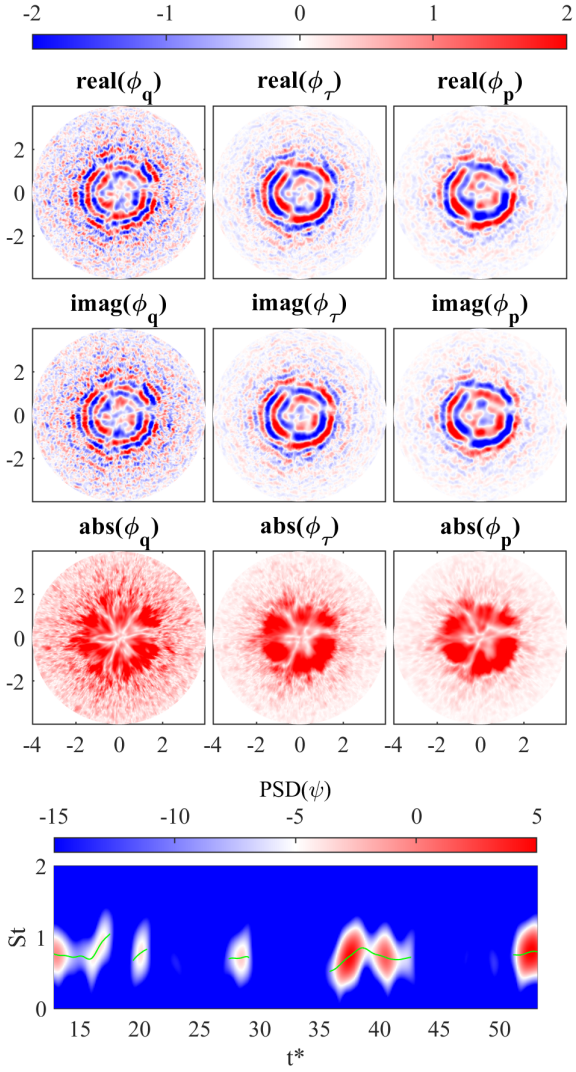


Figure 3. 2nd LSE-HPOD mode. Spatial patterns of Nu (1st column), τ_w (2nd column) and p (3rd column), represented as real (1st row), imaginary (2nd row) and absolute value (3rd row) parts. Spectrogram of the temporal pattern (4th row).

waves being the footprint on the wall of ring vortex structures in the flow. Modes/wavenumbers with a lower impact on the std seem to extend further, possibly indicating a contamination of the effect of the ring vortices with other effects. As already commented, the waves representing different wall quantities reported in Fig. 6 recover a very similar radial wave pattern but with a phase shift between them. In particular τ_w waves are advanced in phase of roughly $\pi/2$ with respect to their Nu counterpart. This is better visualized by including a $-\pi/2$ phase shift to the τ_w wave and rescaling by the maximum of the envelope, as reported in Fig. 8, showing a good match between corresponding waves. This phase shift is compatible with the maximum heat transfer happening in the nodes of the τ_w waves. Considering that these waves are the footprint of impinging vortices on the wall, it can be speculated that maximum heat transfer would occur in the stagnation region induced by the fluid being pushed towards the wall by the ring vortices. The presence of a stream of fluid directed towards the wall, however, should induced by a positive pressure at the wall. Fig. 8 reports also the waves of negative pressure, showing that these waves are not in phase-opposition with the Nu waves, but are advanced in phase of roughly $\pi/4$, suggesting that the hypothesis drawn before is flawed. A more detailed analysis, involving the decomposition of the full 3D flow field instead of 2D wall maps, would be required in the future to identify the reasons behind this discrepancy.

5 Conclusions

In this work, we analyzed the relation between instantaneous heat and momentum transfer in an impinging jet. The data used in the analysis proceed from a DNS of an impinging jet with a nozzle-to-plate distance of 2D, Re=5300 and Pr=1. The analysis focuses on the footprint of the travelling flow features which impact on the wall and are advected radially. In order to isolate these features, the space-only HPOD, applied in the radial direction, has been applied on the instantaneous Nusselt number maps. The effect of these waves on the wall shear stress and on the wall pressure has been estimated using LSE, which allows to extract from the dataset the part temporally correlated with the waves. The HPOD retrieves Nu waves with low azimuthal wavenumber component and which propagates radially. These waves are subjected to a strong modulation in the radial direction, in particular showing high activity

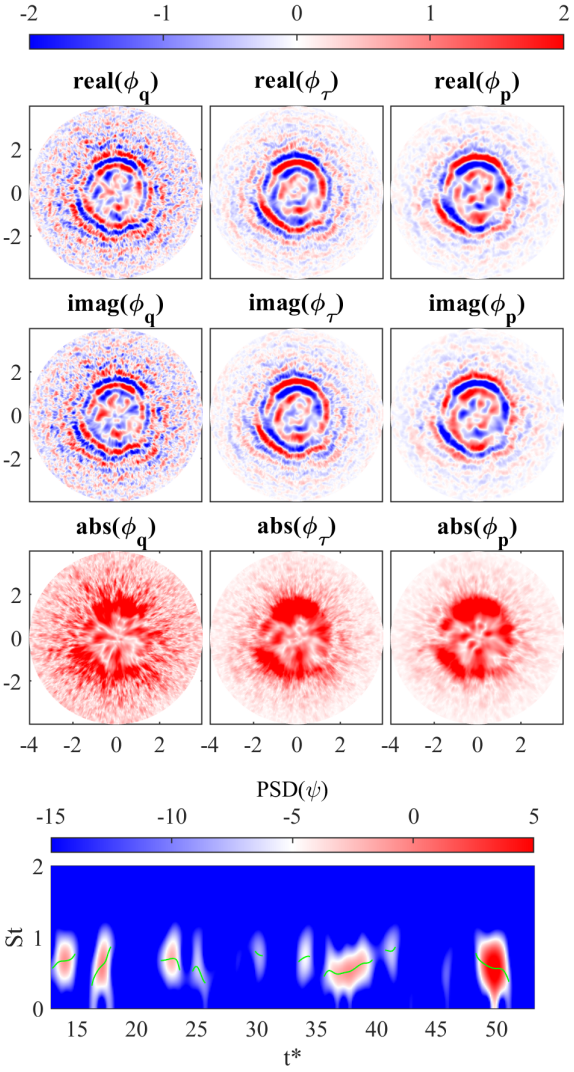


Figure 4. 3rd LSE-HPOD mode. Spatial patterns of Nu (1st column), τ_w (2nd column) and p (3rd column), represented as real (1st row), imaginary (2nd row) and absolute value (3rd row) parts. Spectrogram of the temporal pattern (4th row).

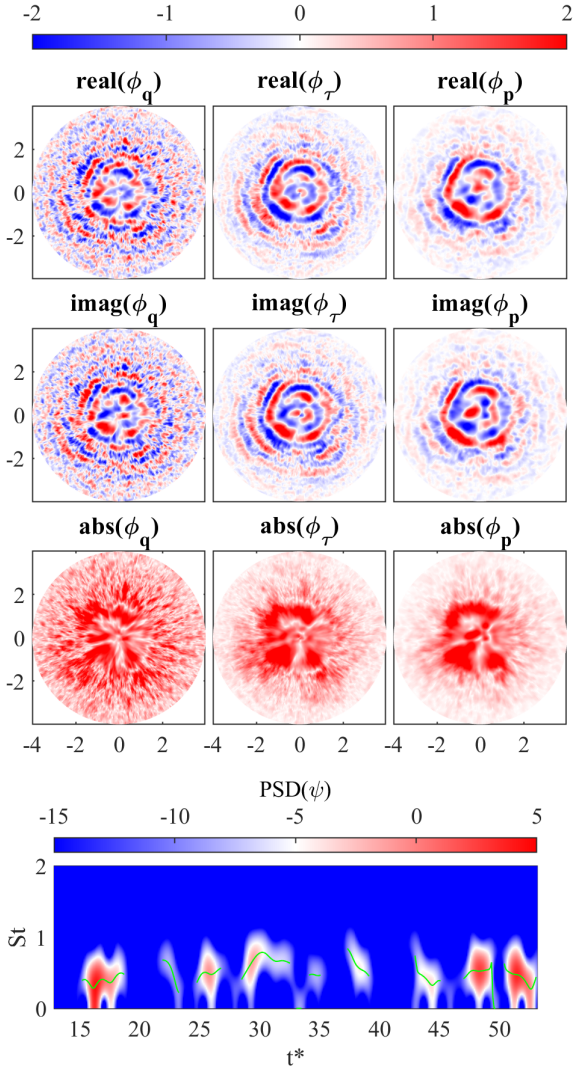


Figure 5. 4th LSE-HPOD mode. Spatial patterns of Nu (1st column), τ_w (2nd column) and p (3rd column), represented as real (1st row), imaginary (2nd row) and absolute value (3rd row) parts. Spectrogram of the temporal pattern (4th row).

in the region between 1D and 2D from the jet impingement point. The temporally correlated features of τ_w and p show a matching behavior. The main difference with the *Nu* waves is a phase delay of the "carrier" wave, corresponding to a phase advance of 45° and 90° respectively for the negative pressure waves and the wall shear stress. In contrast, the modulation behavior and the azimuthal wavenumber content is kept relatively similar between these waves and the wall heat transfer waves. Due to the time/space duality of travelling waves, the phase delay angle observed in the spatial patterns can be interpreted as a phase advance angle in time, i.e. that the travelling wave of τ_w and $-p$ are, respectively, $\pi/2$ and $\pi/4$ in advance in time with respect to the one of Nu. This suggests that a similarity between heat and momentum transfer might hold for time-varying quantities, but requires to account for possible delays between the 2 phenomena. However, while the phase quadrature relation between Nu and τ_w structures might suggest that the maximum heat transfer occurs in the regions of zero wall shear stress, i.e. half a wavelength after the passage of a vortex ring, the $\pi/4$ shift on the pressure seems to suggest a more complex relation between the passage of flow structures and their footprint on the wall.

Acknowledgments

This work was supported by the German Research Foundation (DFG) under the Collaborative Research Centre TRR150 (project number 237267381) and by the Alexander von Humboldt-Foundation. The simulations were performed on the HPE Apollo (Hawk) supercomputer at the High Performance Computing Center Stuttgart (HLRS) under the grant number 44198.

REFERENCES

Borée, J. 2003 Extended proper orthogonal decomposition: a tool to analyse correlated events in turbulent flows. *Experiments in Fluids* **35** (2), 188–192.

Dong, S. 2015 A convective-like energy-stable open boundary condition for simulations of incompressible flows. *Journal of Computational Physics* **302**, 300–328.

Jambunathan, K., Lai, E., Moss, M. A. & Button, B. L. 1992 A review of heat transfer data for single circular jet impingement. *International Journal of Heat and Fluid Flow* **13** (2), 106–115.

Liu, X., Xie, Z. & Dong, S. 2020 On a simple and effec-

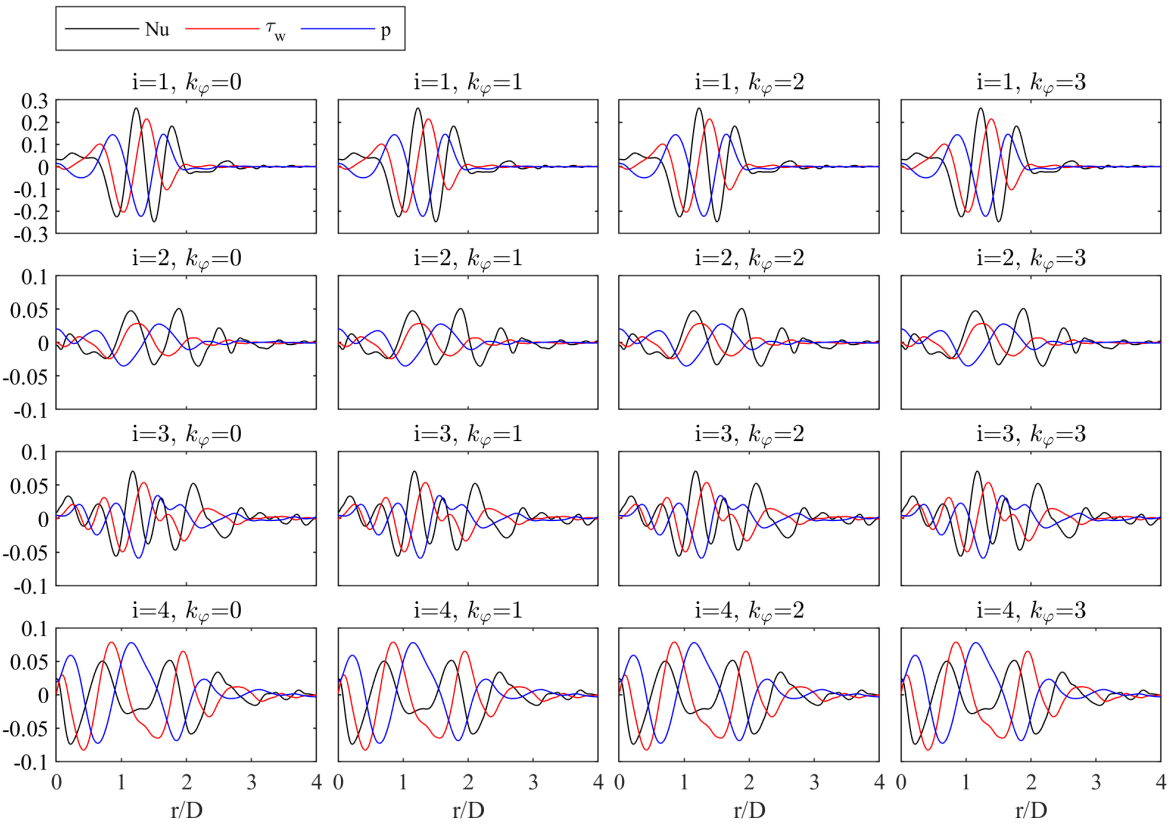


Figure 6. Wavepatterns extracted from the Fourier decomposition in the azimuthal direction of the LSE-HPOD spatial patterns. Mode numbers i from 1 to 4 (rows) and azimuthal wavenumbers k_θ from 1 to 4 (columns).

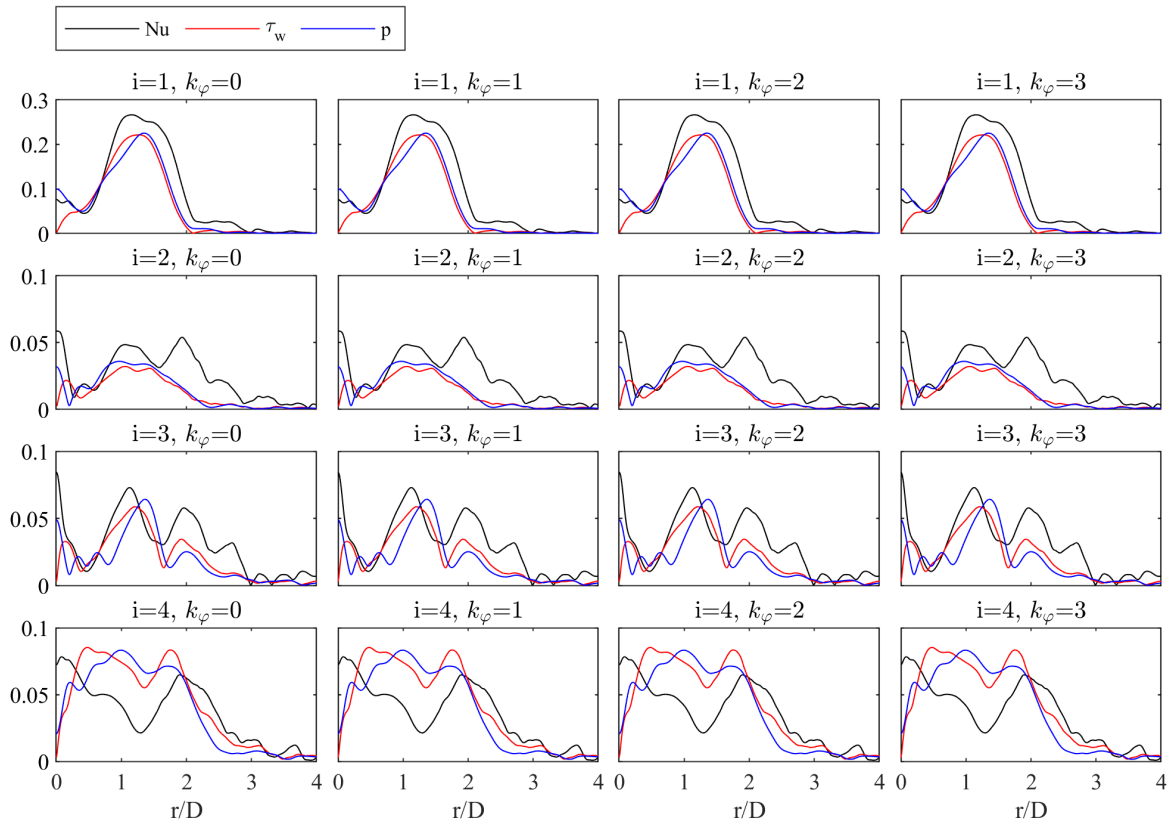


Figure 7. Envelopes of the wavepatterns extracted from the LSE-HPOD spatial patterns. Mode numbers i from 1 to 4 (rows) and azimuthal wavenumbers k_θ from 1 to 4 (columns).

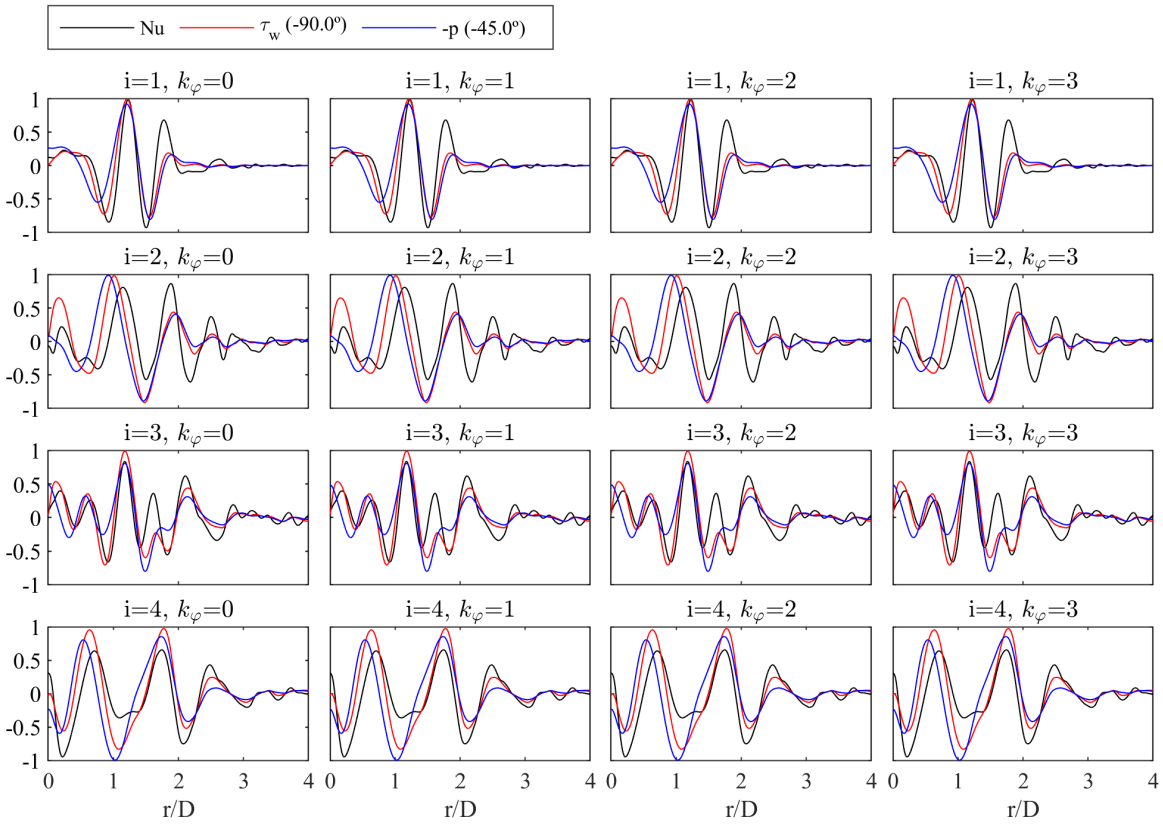


Figure 8. Wavepatterns extracted from the LSE-HPOD spatial patterns after phase-shifting (by $-90°$ and $-45°$ for wall friction and pressure waves, respectively) and rescaling with envelope maxima. Mode numbers i from 1 to 4 (rows) and azimuthal wavenumbers k_θ from 1 to 4 (columns).

tive thermal open boundary condition for convective heat transfer problems. *International Journal of Heat and Mass Transfer* **151**, 119355.

Raiola, M. & Kriegseis, J. 2026 Hilbert proper orthogonal decomposition: A tool for educing advective wave packets from flow field data. *Physical Review Fluids* **11**, 044905.

Rönnberg, K. & Duwig, C. 2021 Heat transfer and associated coherent structures of a single impinging jet from a round nozzle. *International Journal of Heat and Mass Transfer* **173**, 121197.

Wilke, R. & Sesterhenn, J. 2017 Statistics of fully turbulent impinging jets. *Journal of Fluid Mechanics* **825**, 795–824.

Woodworth, A. D., Salazar, D. M. & Liu, T. 2023 Heat transfer and skin friction: beyond the reynolds analogy. *International Journal of Heat and Mass Transfer* **206**, 123960.